# Indium Doped ZnO as Efficient Photo-sensitive Material for Sunlight Driven Hydrogen Generation and DSSCs applications: Integrated Experimental and Computational Approach

RatnaChauhan[a], Manish Shinde[b],YogeshSethi[b],YogeshWaghadkar[a], Sachin R. Rondiya[c], Nelson Y. Dzade[c], Suresh Gosavi[d*] and Mohd. Muddassir[e]

[a]Department of Environmental Science, SavitribaiPhule Pune University, Pune-411007, India.

[b]Centre for Materials for Electronics Technology (C-MET), Panchawati, Pune-411008, India.

[c]School of Chemistry, Cardiff University, Main Building, Park Place, Cardiff, CF10 3AT, United Kingdom.

[d]Department of Physics, SavitribaiPhule Pune University, Pune-411007, India.

[e]Department of Chemistry, College of Science, King Saud University, Riyadh 11451, Saudi Arabia.

Email: swg@physics.unipune.ac.in

## Abstract

Electricity generation using simple and cheap dye sensitized solar cells and photocatalytic water splitting to produce future fuel, hydrogen, directly under natural sunlight fascinated the researchers world-wide. Herein, synthesis of indium doped wurtzite ZnO nanostructures with varying molar percentage of indium from 0.25 to 3.0% with concomitant characterization indicating wurtzite structure is reported. The shift of (002) reflection plane to higher 2θ degree with increase in indium doping thus is a clear evidence of doping of indium in zinc oxide nanoparticles. Surface morphological as well as microstructural studies of In@ZnO exhibited generation of ZnO nanoparticles and nanoplates of diameter 10-30 nm. The structures have been correlated well using computational density functional theory (DFT) studies. Diffuse reflectance spectroscopy depicted the extended absorbance of these materials in the visible region. Hence, the Photocatalytic activity towards hydrogen generation from water under natural sunlight as well as efficient DSSC fabrication of these newly synthesized materials has been demonstrated. In-doped ZnO exhibited enhanced photocatalytic activity towards hydrogen evolution (2465 μmol/h/g) via water splitting under natural sunlight. DSSC fabricated using 2% In-doped ZnO exhibited an efficiency of 3.46 % which is higher than other reported In-doped ZnO based DSSCs.

**Keywords:** Photocatalyst, Indium doped ZnO nanostructures, hydrogen generation, DFT studies, DSSCs

## Highlights:

- Indium doped wurtzite ZnO nanostructures with varying molar percentage of indium synthesized.
- Indium doping into ZnO was confirmed by XRD, XPS and FETEM and corroborated by DFT studies
- DFT studies show an increase in the band gap with increasing indium concentration.
- In-doped ZnO exhibited enhanced photocatalytic activity towards hydrogen evolution (2465 μmol/h/g)
- DSSC fabricated using 2% In-doped ZnO exhibited an efficiency of 3.46 %

## Introduction

During the last few decades, the rise in temperature of earth also termed as "Global Warming" is due to air pollution occurring because of the uncontrolled emission of greenhouse gases *viz.* carbon dioxide, carbon monoxide, etc. Global warming causing greenhouse gases can be reduced only when the production and supply of secure, clean and sustainable energy will be practiced [1]. The rapid growth in the World's population and depletion of fossil fuel prompted materials scientists and chemists to explore alternative energy sources which can prove to be cost effective, eco-friendly alternative to the conventional energy resources [2]. Also, these alternative energy sources should not generate harmful by-products which may lead to secondary pollutants [2]. Some renewable energy sources are solar cells, wind, biomass and water, which are capable of catering 88% of global energy demand. Hydrogen is good alternative energy source of biomass and can prove to be a probable substitute of fossil fuel [3]. This is because it possesses high energy density (120-140 MJ $kg^{-1}$) is clean, eco-friendly and non-toxic but highly inflammable in nature. Solar cells, especially, based on dye sensitization of semiconductor nanoparticles known as dye sensitized solar cells (DSSCs) is a simple, cost effective and less environmentally damaging alternative than conventional silicon solar cells. Even though its efficiency is less at present, it can be useful for certain low cost equipment like toys, flexible gadgets and as DSSC windows for buildings and malls.

Utilizing solar energy for photocatalytic production of hydrogen on photocatalyst surface is one of the promising alternative to resolve the current energy and environmental crisis [4-6]. In view of this, the production of hydrogen by employing photocatalytic materials have been demonstrated since 1972 [7]. Henceforth, myriad of semiconducting materials have been explored to assess their potential as photocatalyts for efficient hydrogen production [8-10]. An important prerequisite of this quest is to identify materials with optimal band structure that can promotecharge separation and remain stable against photocorrosion with unaltered structural integrity after prolonged application. Apart from the composition and the molecular arrangement, the morphological dimension of such material too is the key aspect. Illuminating a photocatalytic surface with energy greater than or equal to its band gap leads to the creation of electron−hole pairs [11]. These photogenerated charge carriers produced within the nanostructure are required to react with water molecules existing on the photocatalyst's surface. In this process of reaching the surface, the

charge carriers undergo recombination or get trapped at defect sites. Hence the characteristics of good and efficient photocatalyst are: (1) They must have the ability to provide better charge transfer mobility; (2) incorporation of the facile synthetic process with an efficient reaction mechanism and (3) the importance of photons to impeach the nano-architectures to reach the photoactive sites [12].

The use of semiconducting materials for hydrogen generation and DSSC fabrication is an extremely economical and efficient technique. Several chemical and physical methods have been employed for synthesis of targeted materials *viz.* hydrothermal, solvothermal, co-precipitation method, sol-gel, etc. Among these techniques, the hydrothermal is highly efficient, easy, and less expensive bottom-up technique. Various semiconductors had been used as photo-catalyst as well as photoanodes in DSSCs. Most of researchers focused on to the development of highly efficient and chemically stable photocatalyst, such as $TiO_2$, ZnO, carbon dot, $Nb_2O_5$, $SnO_2$ and some composite materials. However, some of these catalysts possess band gaps in UV (3-4% of solar spectrum) region and as a consequence the major part of solar spectrum (visible region ~55%) remains unutilized which eventually results in their less photocatalytic activity. Hence,in order to enhance the photocatalytic activity, it is necessary to shift the band gap from UV region to visible region and this can be achieved by doping these materials with materials such as C, N, S, Sn, Co, Fe, In, etc [13].Because of doping with such materials, the rate of electron-hole recombination declines which in turn improves their photocatalytic activity as well as DSSC efficiency. Among these materials, indium has been reported as a highly proficient dopant which can shift the band gap of ZnO to visible region and inhibits the fast recombination of electron-hole pairs [14-15].

Keeping these worthy facts in mind and in the quest of new doped materials for their plausible photocatalytic splitting of water for targeted hydrogen generation, in the investigation presented herewith, indium doped ZnO nanoparticles have been synthesized hydrothermally and their application as photocatalyst in hydrogen generation has been studied. In addition, DSSCs based on In-doped ZnO nanostructures were also fabricated

## Experimental

### Synthesis of Indium doped ZnO

The aqueous solutions of 0.2 molzinc acetate in 100 mL of distilled water were prepared which were having varying quantities of indium acetate (0.25 to 3mol%). After 10 minutes of stirring,0.2

M of citric acid and 10 mL of 1 M NaOH solution were added to the solution mixture and then the mixture was stirred for 30 min at80 $^{o}$C. After that the mixture was transferred to Teflon lined stainless steel container and the assembly was kept into the oven at 180 $^{o}$C for 24 h. Thereafter, the obtained white/grey precipitate was washed thrice with deionized water and dried in oven at 50 $^{o}$C, annealed at 450 $^{o}$C in air to get indium doped ZnO powder samples. The synthesis of pristine ZnO was also executed in the similar manner.

**Instrumentation**

Structural information of the In-doped ZnO powder samples was acquired using X-ray diffractometer (Bruker, D8, ADVANCE, Germany) with Ni-filtered $CuK_{\alpha}$ radiation ($\lambda$ = 1.54 Å). Surface morphological features In-doped ZnO powder samples were determined by obtaining Field Emission Scanning Electron Microscopy (FESEM) images using Hitachi, Japan SEM model no. S-4800. For this purpose, the typical synthesized In-doped ZnO powder sample was directly sprinkled on the conducting carbon tape stuck to aluminum stub. Finally, it was sputter coated with ultra-thin conducting gold film to reduce the effects arising due to charging. X-ray photoelectron spectroscopy (XPS) was used to investigate the composition of the products and confirm the oxidation state of the elements, performed on PHI5000 Versa Probe III. The photovoltaic parameters, short-circuit current ($J_{sc}$, mA cm$^{-2}$), open-circuit voltage ($V_{oc}$, V), fill factor (FF), and energy conversion efficiency ($\eta$) of DSSCs were determined by using a digital Keithley 236 mm under an irradiation of white light (1000 W/HS Xenon arc lamp) with light intensity of 100 mW cm$^{-2}$ at 1.5 AM. The current measured in positive forward bias condition and obtained positive current with respect to reference and counter (both are clubbed together). The incident photon-to-electron conversion efficiency (IPCE) was measured by using a 300 W Xe lamp light source attached to a monochromator (Oriel). A reference Si photodiode calibrated for spectral response was used for the monochromatic power density calibration.

**Computational details**

The first-principles density functional theory (DFT) calculations were performed using the Vienna Ab initio Simulation Package (VASP) [16-18]. The interactions between the core and valence electrons were treated using the Project Augmented Wave (PAW) method [19].The electronic wave functions are expanded on a plane-wave basis set with a cutoff energy of 600 eV. Geometry optimizations were performed using the conjugate-gradient algorithm until the residual Hellmann–

Feynman forces on all relaxed atoms reached $10^{-3}$ eVÅ$^{-1}$. The electronic exchange–correlation potential was calculated using the Perdew–Burke–Ernzerhof (PBE) generalized gradient approximation (GGA) functional [20]. Long-range vdW interactions were accounted for using method of Grimme (DFT-D3) [21]. The ZnO was modelled in the hexagonal wurtzite phase. A large 3×3×2 supercell containing 72 atoms had been used to investigate different concentrations of In-doping and to reduce the interactions between dopants with their images in the neighbor cells. A Monkhorst-Pack *k*-point mesh of 3×3×3 was used to sample the Brillouin zone of the pure and doped supercell structures [22-23]. To accurately predict the band gaps of the investigated materials, the screened hybrid functional HSE06 [24] was used with the exchange values of 25%. The projected density of states (PDOS) was calculated using tetrahedron method with Bloch correction [25].

**Visible light photocatalytic hydrogen generation from water**

Photocatalytic hydrogen generation was carried out at room temperature under sunlight using 100 mL of double distilled water and 25 mL of methanol as a sacrificial reagent and 0.1g photocatalyst in a 250 mL round bottom flask. ZnO and In@ZnO photocatalysts were added with 0.5 wt% preloaded platinum as a co-catalyst. Argon gas was purged through this reaction mixture in order to remove the dissolved gases. A round bottom flask (250 mL) was connected to the graduated measuring gas collector tube. The gas collector tube had a septum arrangement to get rid of the evolved gas through a gas tight syringe and to measure the amount of gas evolved. The amount of gas evolved was noted with time. The purity of the collected gas was analysed using gas chromatography (Model Shimadzu GC-14B, MS-5 Å column, TCD, Ar carrier).

**Electrodes preparation and DSSC Fabrication**

The conductive glass substrates (FTO) were cleaned with ethanol, deionized (DI) water and acetone and then dried. The pastes were prepared by using as synthesized In@ZnO, α-terpinol, ethyl cellulose and ethanol. The photoanodes on FTO were prepared by using doctor's blade techniques and annealed at 450 $^{o}$C for 30 min in air at the rate of 4 $^{o}$C/minute. The annealed In@ZnO electrodes were then immersed in to the 0.3 mM solution of N719 dye in aacetonitrile/tert-butyl alcohol solvent mixture for 12 h. The non-adsorbed dye was washed off with anhydrous ethanol. The platinum paste was used as the source of platinum electrode. The platinum paste were spread on FTO by screen printing technology and the annealed in tubular

furnace at 400 °C for half an hour in air with the rate of 4 °C/minute. The sandwich assembly of DSSCs was fabricated by placing both electrodes photoanode and counter anode one over the other in face to face sandwich manner. This sandwich assembly was then sealed with the sealant leaving one side open through which the electrolyte solution was injected between the electrodes followed by sealing with sealant and make electrical contact on both electrodes by using copper wires, silver paste and araldite.

## Results and Discussion

### Characterization of ZnO and Indium doped ZnO

#### *X-ray diffraction pattern*

XRD patterns of pure zinc oxide and indium doped zinc oxide samples are shown in Fig. 1a.All the XRD patterns matched well with the wurtzite structure ZnO (JCPDS file No. 80-0075). Indium doped ZnO nanoparticles also possess the wurtzite structure similar to ZnO which may be attributed to although both possess different ionic radii $In^{3+}$ (0.62 Å) and $Zn^{2+}$ (0.74 Å). As a result, the XRD patterns of indium doped zinc oxide nanoparticles exhibited shift in (002) reflection towards higher angle (see the inset in Fig. 1b) due to increase in the *d*-spacing with increase in the indium acetate concentration. This shift in (002) reflection is an evidence for doping of indium in zinc oxide. Apart from this, the crystallite size of pure zinc oxide was found to be smaller in comparison with that of indium doped zinc oxide nanostructures.

#### *FESEM imaging*

FESEM images of undoped and indium doped ZnO powder samples are shown in Fig. 2. In case of undopedZnO powder sample, wide particle size distribution can be seen (Fig. 2a). There are many nanoscale particles having spherical and faceted morphology having size in the range of 20-100 nm. However, many submicron sized particles having faceted rod and sheet, like morphology are also noticed. In case of In-doped ZnO samples, with increase in the doping concentration, particles size distribution has narrowed and number of submicron sized rod and sheet like particles got reduced (Fig. 2b, 2c, 2d, 2e and 2f). Additionally, with increase in doping concentration, the particle surface tended to become smoother rather than showing faceted sharp edges. In case of ZnO sample prepared with 2% indium doping (Fig. 2e), spherical and irregular shaped nanoparticles having smooth surface and size in the range of 20-50 nm are seen. As seen from the FESEM images, significant variation the particle size is not observed which in turn could lead to

a substantial change in the band gap (indicated by the blue shift in UV-visible spectra). Thus, the observed blue shift in ZnO is attributed to indium doping only.

**FETEM-STEM-EDS-Elemental Mapping**

The FETEM images ZnO nanopowder sample comprising of2mol%Indiumis shown in Fig. 3. The low magnification image (Fig.3a) showed the formation of agglomerated nanoparticles with nearly uniform size particles. Formation of spherical nanoparticles with size in the range of 10-20 nm was revealed from the FETEM image obtained at intermediate scale magnification (Fig.3b). High magnification (Lattice) image (Fig.3c) disclosed that each individual particle exhibited crystalline orientation to a particular direction thus giving overall nanocrystalline characteristic to the sample. This is further corroborated by the selected area electron diffraction (SAED) pattern (Fig. 3d) which revealed a rather nanocrystalline pattern as compared to polycrystalline pattern of regular thick rings [26].

The energy dispersive spectroscopy (EDS) analysis of the same sample (Fig.4) revealed a zinc deficient stoichiometry. Presence of 1.82 atomic percent of indium is close to 2 mol% dopant precursor. To further probe the distribution of indium in the sample, FETEM-STEM-EDS-elemental mapping study was also performed. The overlap of elements such as indium (Fig.5b), zinc (Fig.5c) and oxygen (Fig.5d) with the corresponding electron image (Fig.5a) confirmed their uniform distribution throughout the sample. The colour intensity of the image corresponding to indium (Fig.4b) can be seen to below because only ~2% doping had been done. Overall, the images substantiate the uniform doping of indium in the sample.

**UV-Visible and photoluminescence spectroscopy**

UV-Visible spectra of indium doped zinc oxide nanostructures show blue shift in their band gaps with respect to pristine ZnO (Fig. 6a). The band gap in indium doped ZnO increases from 3.38 eV (pure ZnO) to 3.58 eV with rise in the indium doping concentration. The observed blue shift inZnO is attributed to indium doping but not to the change in particlesize. The photoluminescence spectra of indium doped ZnO exhibit two emission bands (Fig. 6b); one at 385 nm is due to the near band edge emission of ZnO while other observed at ~550 nm is arising because of the oxygen vacancies. The emission band at ~385 nm is due to excitonic recombination in ZnO. The intensity of near band emission band is lower in indium doped ZnO samples at all concentrations of indium as

compared to that of pure ZnO. The decline in emission intensity after indium doping is because of the weak excitons (Coulomb interaction effect) [27]. The emission band at ~ 550 nm corresponds to oxygen vacancies and the intensity of this band decreases after doping of indium in the zinc oxide hierarchical nanostructures. This can be attributed to the reduction in number of oxygen vacancies. The visible emission of zinc oxide nanoparticles is usually observed as a broad band at room temperature and this blue-green region had been reported as related to the surface defects, such as oxygen vacancies [28-29]. The ionizationstate o f the vacancies imposes strong impact on theintensity of visible emission. Since the PL emissions mainly due to the recombination of photogenerated electrons and holes, the decline in the emission intensity in In@ZnO thus indicates inhibition of electron–holerecombination due to the co-catalytic effect in In@ZnO. This lengthens the lifetime of charge carriers and is beneficial for the improvement of photocatalytic activity.

**First-principles density functional theory (DFT) calculations**

The experimental estimated band gaps have been further corroborated by first-principles DFT-based theoretical calculations. A large 3×3×2 supercell with 72 atoms was used to investigate different level of indium doping and to reduce the interaction between dopants with their images in the neighbor cells. By substituting zinc atom by one and two Indium atoms resulted in the In-doped ZnO with compositions $Zn_{0.97}In_{0.03}O$ and $Zn_{0.94}In_{0.06}O$, respectively. The optimized structures of the pure and In-doped ZnO materials are shown in Fig. 7 (a-c). The lattice parameter of the fully relaxed 3×3×2 supercell of the pure ZnO is predicted at $a$=9.821 and $c$=10.481 Å, compared to $a$= 9.858Å and $c$= 10.621 Å for $Zn_{0.97}In_{0.03}O$ and $a$= 9.889 and $c$= 10.660 Å for $Zn_{0.94}In_{0.06}O$. These results indicate that the substitution of Zn by Indium causes small expansion in the lattice in good agreement with the smaller ionic radius of $In^{3+}$ (0.62 Å) than $Zn^{2+}$ (0.74Å). The corresponding electronic density of states (DOS) projected onto the Zn, In and O ions is shown in Fig.7(d-f). The calculated band gaps of ZnO, $Zn_{0.97}In_{0.03}O$, and $Zn_{0.94}In_{0.06}O$ are 3.24, 3.38, and 3.49 eV, respectively which indicate increase in band gap parameter with rise in indium concentration. Compared to the pure ZnO, the substitution of Zn by indium caused the valence band to shit to lower energy levels, with the Indium atoms introducing small DOS at the top of the valence band.

## XPS study

To further confirm the doping of indium into In@ZnO nanoparticles, XPS analysis was performed (Fig. 8). The In 3d spectrum of In@ZnO nanoparticles is shown in Fig. 8 (a). The appearance of Indium spectrum and the absence of the $In_2O_3$ phase in the previous XRD patterns suggest that Indium element is doped into the ZnO crystal. In addition, compared to the ZnO sample, the Zn $2p_{3/2}$and Zn $2p_{1/2}$peaks of In@ZnO shifted slightly towards a higher binding energy (as shown in Fig. 8 (b). The peak shifts can be explained by the difference in the electronegativity of Indium (c ¼ 1.78) and Zn (c ¼ 1.65). Because of the higher electronegativity of In than Zn, the valence electron density of Zn in the Zn–O–In bond in the In@ZnO nanoparticles sample becomes lower than that in the Zn–O–Zn bond in the ZnO sample. Consequently, the screening effect of Zn in the In@ZnO nanoparticles sample is weakened, and the binding energy of Zn 2p increases. The O 1s deconvoluted spectra of the ZnO and In@ZnO are shown in Fig. 8(c). The low binding energy peak (OI) corresponds to $O_2$ combined with metal ions in the ZnO and In@ZnO. The medium binding energy peak (OII) is related to the oxygen deficiency in the ZnO and In@ZnO, indicating the corresponding oxygen vacancy concentration. The high binding energy peak (OIII) is ascribed to some chemisorbed oxygen components such as $–CO_3$ and $H_2O$. Also, the O 1s peak of In@ZnO shifts slightly towards a higher binding energy as compared to that of the undoped ZnO sample. The shift is also due to the higher electronegativity of indium In (III) ion than Zn (II) ion, as abovementioned. An intensity ratio of OII/Ototal has been obtained to compare the relative concentration of the oxygen vacancies: the values are 0.29 and 0.31 for the ZnO and IZO nanorod samples, respectively. The In@ZnO sample with a higher value has more oxygen vacancies than ZnO because of the lower bond strength of In–O as compared to that of Zn–O. On the basis of these results, the Indium element is doped into the ZnO crystal, which would generate more oxygen vacancies; therefore, a higher carrier concentration can be obtained for the In@ZnO.

## Photocatalytic Study

### Photocatalytic $H_2$ evolution from $H_2O$ Splitting using In@ZnO nanostructures

The photocatalytic hydrogen ($H_2$) generation from water ($H_2O$) splitting was performed using as synthesized ZnO and In@ZnO nanostructure as a photocatalyst under natural sun-light. In the present study, we used methanol as a sacrificial reagent along with that of 0.5 wt % Pt loaded on ZnO and In@ZnO nanostructures in 100 mL DI water. Pt acts as a co-catalyst [30] and it provides

smaller barrier for migration of electrons from semiconductor photocatalyst i.e. captures the photoexcited electrons in the conduction band of the ZnOand In@ZnO nanostructures, it suppresses the electron–hole pairs recombination rate which results in enhancement of the photocatalytic activity [31].The photocatalytic $H_2$ evolution as a function of time is shown in Fig. 9. The $H_2$ generation data for all samples is summarized in Table 1. Among all the tested samples In@ZnO having 2% indium doping showed maximum hydrogen evolution rate of 2465 µmol/h/g.However, the photocatalytic activity declined with rise in indium content above 2%, i.e., the photocatalytic activity of 3%In@ZnOwas lower than that of 2%In@ZnO. This indicates that higher indium content beyond 2%is unfavorable for the photocatalytic $H_2$ production process [32-33]. This observation suggested that In@ZnO nanostructure exhibits higher photocatalytic activity than pure ZnO, and commercial P25, $TiO_2$photocatalysts [34-35]. The photocatalytic reactions can be described as follows,

$$In@ZnO \xrightarrow{hv} e^- + h^+ \text{..... (1)}$$

$$H_2O + 2h^+ \rightarrow HO^* + H^+ \text{..... (2)}$$

$$CH_3OH + OH^* \rightarrow *CH_2OH + H_2O \text{.....(3)}$$

$$*CH_2OH \rightarrow HCHO + H^+ + e^- \text{..... (4)}$$

$$2H_2O + e^- \rightarrow H_2 + 2OH^- \text{..... (5)}$$

$$\text{Overall } CH_3OH \xrightarrow{\text{Catalyst/hv}} H_2 + HCHO \text{..... (6)}$$

As far as photocatalytic activity of In doped Zno nanostructures is concerned, there are reports on photocatalytic degradation of organic compounds but very few reports are available on photocatalytic hydrogen generation [36-40]. M.G. Nolan et al reported UV light assisted stearic acid degradation as a function of UV irradiation time for nanostructured In doped ZnO (3 at %) thin films that are prepared by aerosol assisted chemical vapour deposition technique at atmospheric pressure on glass substrates [36]. A. Murali etal prepared In doped ZnO nanopowders (4 and 8 at %) by plasma-assisted chemical vapor synthesis technique and studied their photocatalytic methylene blue degradation under UV light [37]. M. Rezapour and N. Talebian synthesized pure and In doped ZnO nanostructures (5 mol %) having morphologies like spheres, Hexagons, flowers and polyhedral using hydrothermal method by varying the surfactants (cationic, anionic and nonionic) [38]. They studied the Photocatalytic degradation of an organic pollutant,

2,4,6-trichlorophenol, under UV as well as visible radiation. They observed that better degradation performance was observed for In doped ZnO nanostructures as compared to pure ZnO, however, better performance was obtained under UV irradiation. In another effort, Y. Yu et al. prepared In doped ZnO nanopowders with rich oxygen vacancy defects via modified co-precipitation method [39]. Quite interestingly, they obtained better photocatalytic activities for their In doped ZnO nanostructures containing rich oxygen vacancy defects under visible light irradiation towards the degradation of methylene blue (MB) and methyl orange (MO) corresponding to 96.84% and 90.05%, respectively. S. B. Ameur et al grew thin films of undoped ZnO, (1%) Co doped ZnO and (1%) In doped ZnO on flexible PEI (Polyetherimide) substrate via spray pyrolysis [40]. They observed that undoped as well as Co and Indoped ZnO thin films exhibited Photocatalytic efficiency against crystal violet dyeup to 80% under either UV light or sunlight when irradiated for 210 min. However, Co doped and In doped ZnO thin film exhibited the better Photocatalytic performance under UV irradiation and under sunlight respectively. In doped ZnO thin film exhibited better photocatalytic efficiency under sunlight due to the narrowing of its optical gap.All these reports attributed the enhancement in the photocatalytic performance of Indoped ZnO nanostructures as compared to pure ZnO to the reduced recombination rate of photogenerated charge carriers due to In doping. However, all these reports pertain to photocatalytic organic compound/pollutant degradation. To the best of knowledge, there are no reports of photocatalytic hydrogen generation via water splitting and this solitary report is thus is the novelty of our work. Nevertheless, in in case of photocatalytic water splitting, the basic principle of operation in photocatalytic hydrogen generation remains the same that is based on the defects due to$In^{3+}$ ions creating several active sites which favour efficient electron–hole separation.

**Photovoltaic Characterization**

**Current-voltage Curve and IPCE**

The current–voltage characteristic curves of DSSC fabricated using Indium doped ZnO and plain ZnO under simulated AM 1.5 light are shown in Figure 10 (a). The photovoltaic parameters for the fabricated DSSCs, measured from current-voltage curve are shown in Table 1. The highest photovoltaic performance obtained with 2% In@ZnO ($J_{sc}$ = 10.08 mA/cm$^2$,$V_{oc}$= -0.566 V, η= 3.46% and fill factor *FF*= 0.60) which is about 2 fold maximum output than the plain ZnO. From the photovoltaic data it is evident that the Indium doping in ZnO enhances the DSSCs

performances. It is also proved that In-doping lowered the recombination resistance and prolonged electron lifetime of the doped films, therefore diminishing the recombination process [41]. It is found that the indium-doping acting as an important role in the formation of ZnO structures and the resulted power conversion efficiency of dye-sensitized solar cells. Doping with 2 wt% indium results in the largest increase in electrical conductance in the ZnO film and yields the best power conversion efficiency [41]. However, indium doped ZnO thin film on non-conducting glass acted as TCO layer in this case.

The photovoltaic parameters like fill factor and conversion efficiency have been calculated by using the equations 7 and 8:

$$FF = \frac{P_{max}}{J_{\mathrm{SC}}(\mathrm{A/cm^2}) \times V_{\mathrm{OC}}(\mathrm{V})} \quad (7)$$

$$\eta(\%) = \frac{J_{\mathrm{SC}} \times V_{\mathrm{OC}} \times FF}{I_{\mathrm{inc}}\ (\mathrm{W/cm^2})} \times 100 \quad (8)$$

The maximum output power ($P_{\max}$) was obtained by choosing a point on *J-V* curve corresponding to which the product of current (*J*) and voltage (*V*) gives maximum value. Here $J_{\mathrm{sc}}$, $V_{oc}$ and $I_{inc}$ are short - circuit photocurrent, open-circuit potential and intensity of incident light (100mW/cm$^2$) respectively.

Figure 10 (b) shows the IPCE spectra of fabricated DSSCs. The maximum efficiency of IPCE spectra follows the resultant trend with the Jsc and η of the respective cell. The IPCE data of the cells revealed the utilization of sunlight in the full visible range (400-700nm). As expected from the current density curve and resultant parameters the cell based on film fabricated by 2% In@ZnO exhibited extensive photocurrent onset and showed marked improvement in IPCE in the region of 400 to 700 nm, compared to the plain ZnO and other doping percentage of Indium in ZnO. The maximum of *IPCE* for DSSC fabricated by Indium doped and plain ZnO in the visible region is located at 530 nm. This is about consistent with the expected local maxima ($\lambda_{\max}$) for the N719 dye ($\lambda_{\max}$ in visible region at 535 nm), both corresponding to a metal-to-ligand charge transfer transition. The IPCE results further confirm that the DSSC based on 2% In@ZnO possesses increased light harvesting efficiency compared to the remaining DSSCs due to its improved active

area for maximum dye loading and maximum conversion efficiency. Recently, there are few reports on DSSCs fabricated using In-doped ZnO and have reported efficiency in the range of 1.0 to 3.4 % (see Table 2) [42-44]. However, in the present case, an efficiency of 3.46 % has been obtained for the DSSC fabricated using 2% In-doped ZnO which is comparable/better than these reports.

## Conclusion

The study, presented herein, focused on the hydrothermal synthesis of different molar percentage (0.25 to 3%) indium doped ZnO nanostructures and their photocatalytic activity towards hydrogen generation from water under natural sunlight. Indium doping into ZnO was confirmed by XRD, XPS and FETEM which was further corroborated by DFT studies. Nanoscale In@ZnO photocatalysts showed enhanced photocatalytic activity as compared tothat of their individual counterparts. The enhanced photocatalytic activity was ascribable to the increased electrical conductivity asit suppressed the electron–hole pair recombination rate which resulted in enhancement of the photocatalytic activityby accelerating charge separation by band gap alignment. Among all the tested samples, 2 mol% In@ZnO showed utmost hydrogen evolution rate i.e. 2465 μmol/h/g. DSSC fabricated using 2% In-doped ZnO exhibited an efficiency of 3.46 %. The results of hydrogen generation as well as DSSC studies exhibited direct experimental evidence for improved photocatalytic and electron-hole recombination activity as well as stability and provided useful guidance for developing an efficient photocatalyst and solar cells which is active under natural sunlight.

## Acknowledgement

Authors RC and YB are grateful to the Department of Science and Technology New Delhi for providing financial support to undertake this work. SRR and NYD acknowledge the UK Engineering and Physical Sciences Research Council (EPSRC) for funding (Grant No. EP/S001395/1). This work has also used the computational facilities of the Advanced Research Computing at Cardiff (ARCCA) Division, Cardiff University, and HPC Wales.

**Conflict of Interest:** Authors have no conflict of interest.

## References:


1. Kulkarni AK, Panmand RP, Sethi YA, Kadam SR, Tekale SP, Baeg GH, Ghule AV, Kale BB (2018) *In situ* preparation of N doped orthorhombic $Nb_2O_5$nanoplates /rGO composites for photocatalytic hydrogen generation under sunlight.Int J Hydrog Energy43:19873-19884

**2.** Sethi YA, Pravee CS, Panmand RP, Ambalkar A, Kulkarni AK, Gosavi SW, Kulkarni MV, Kale BB (2018) Perforated N-doped monoclinic $ZnWO_4$ nanorods for efficient photocatalytic hydrogen generation and RhB degradation under natural sunlight.CatalSciTechnol8:2909-2919

3. Ganguly P, Harb M, Cao Z, Cavallo L, Breen A, Dervin S, Dionysiou DD, Pillai SC (2019) 2D Nanomaterials for PhotocatalyticHydrogen Production. ACS Energy Lett 4:1687−1709

4. Gupta U, Rao C (2017) Hydrogen generation by water splitting using $MoS_2$ and other transition metal dichalcogenides. Nano Energy 41:49−65

5. Teets TS, Nocera DG (2011) Photocatalytic hydrogen production. ChemCommun 47:9268−9274

6. Kumaravel V, Mathew S, Bartlett J, Pillai SC (2019) Photocatalytic hydrogen production using metal doped $TiO_2$: A review of recent advances. ApplCatal B 244:1021−1064

7. Fujishima A, Honda K (1972) Electrochemical photolysis of water at a semiconductor electrode. Nature238:37−38

8. Gratzel M (2001) Photoelectrochemical cells. Nature 414:338-344.

9. Wang X, Maeda K, Thomas A, Takanabe K, Xin G, Carlsson JM, Domen K, Antonietti M (2009) A metal-free polymeric photocatalyst for hydrogen production from water under visible light. Nat Mater 8:76−80

10. Zhou X, Liu N, Schmidt J, Kahnt A, Osvet A, Romeis S, Zolnhofer EM, Marthala VRR, Guldi DM, PeukertW (2017) Noble-Metal-Free Photocatalytic Hydrogen Evolution Activity: The Impact of Ball Milling AnataseNanopowders with $TiH_2$. Adv Mater 29:1604747

11. Ganguly P, Byrne C, Breen A, Pillai SC (2018) Antimicrobial Activity of Photocatalysts: Fundamentals, Mechanisms, Kinetics and Recent Advances. ApplCatalB 225:51-75

12. Teoh W, Scott J, Amal R (2012) Progress in Heterogeneous Photocatalysis: From Classical

Radical Chemistry to Engineering Nanomaterials and Solar Reactors. J PhysChemLett 3:629−639

13. Hao X, Jin Z, Xu J, Min S, Lu G (2016) Functionalization of $TiO_2$ with graphene quantum dots forefficientphotocatalytic hydrogen evolution.SuperlatticesMicrostruct 94:237–244
14. Xu L, Su Y, Chen Y, Xiao H, Zhu L, Zhou Q, Li S (2006) Synthesis and characterization of Indium-doped ZnO nanowires with periodical single_twinstructures. J PhysChem B 110: 6637-6642
15. Pal E, Hornok V, Oszko A, ekany ID (2009) Hydrothermal synthesis of prism-like and flower-like ZnO and indium-doped ZnO structures. Colloids Surf A PhysicochemEng Asp 340: 1-9
16. Kresse G, Hafner J (1994) Theory of the Crystal Structures of Selenium and Tellurium: The Effect of Generalized-Gradient Corrections to the Local-Density Approximation. Phys Rev B 50:13181-13185
17. Kresse G, Joubert D (1999) From UltrasoftPseudopotentials to the Projector Augmented-Wave Method. Phys Rev B 59:1758–1775
18. Kresse G, Furthmüller J (1996) Efficient Iterative Schemes for ab initio Total-Energy Calculations using a Plane-Wave Basis set.Phys Rev B 54:11169–11186
19. Blöchl PE (1994) Projector Augmented-Wave Method. Phys RevB 50:17953–17979
20. Perdew JP, Burke K, Ernzerh M (1997) Generalized Gradient Approximation Made Simple.Phys Rev Lett 78:3865-3868
21. Grimme S, Antony J, Ehrlich S, Krieg S (2010) A consistent and accurate ab initio parametrization of density functional dispersion correction (DFT-D) for the 94 elements H-Pu. J ChemPhys 132:154104
22. Kohn W, Sham LJ (1965) Self-consistent equations including exchange and correlation effects. Phys Rev140:A1133–A1138
23. Monkhorst HJ, Pack JD (1976) Special Points for Brillouin-zone Integrations. Phys Rev B 13:5188-5192

24. Krukau AV, Vydrov OA, Izmaylov AF, Scuseria GE (2006) Influence of the Exchange Screening Parameter on the Performance of Screened Hybrid Functionals. J ChemPhys 125:224106

25. Blöchl PE, Jepsen O, Andersen OK (1994) Improved Tetrahedron Method for Brillouin-Zone Integrations. Phys Rev B 49:16223-16233

26. Chen L, Liu Y, Dietz-Rago N, Shaw LL (2015) Bottom-up, hard template and scalable approachestoward designing nanostructured $Li_2S$ for highperformance lithium sulfur batteries.Nanoscale 7:18071-18080

27. Farid S, Mukherjee S, Sarkar K, Mazouchi M, Stroscio MA, Dutta M (2016) Enhanced optical properties due to indium incorporation in zinc oxide nanowires. ApplPhyLett 108:021106

28. Fu YS, Du XY, Kulinich SA, Qiu JS, Qin WJ, Li R, Liu J (2007) Stable aqueous dispersion of ZnO quantum dots with strong blue emission via simple solution route. J Am ChemSoc 129:16029-16033

29. Lv Y, Xiao W, Li W, Xue J, Ding J (2013) Controllable synthesis of ZnOnanoparticles with high intensity visible photoemission and investigation of its mechanism. Nanotechnology 24:175702

30. Liao CH, Huang CW, Wu JCS (2012) Hydrogen Production from Semiconductor-based Photocatalysis via Water Splitting.Catalysts 2:490-516

31. Kulkarni AK, Praveen CS, Sethi YA, Panmand RP, Arbuj SS, Naik SD, GhuleAV, Kale BB (2017) Nanostructured N-doped orthorhombic $Nb_2O_5$asan efficient stable photocatalyst for hydrogengeneration under visible light.Dalton Trans 46:14859-14868

32. Sun S, Gao P, Yang Y, Yang P, Chen Y, Wang Y(2016) N-Doped $TiO_2$Nanobelts with Co-exposed (001) and (101) Facets and Their Highly Efficient Visible-Light-Driven Photocatalytic Hydrogen Production.ACS Appl Mater Interfaces 8:18126-18131

33. Wang L, Wang W(2012) *In situ* synthesis of CdS modified $CdWO_4$nanorods and their application in photocatalytic $H_2$ evolution. CrystEngComm 14:3315-3320

34. Apte SK, Garaje SN, Mane GP, Vinu A, Naik SD, Amalnerkar DP, Kale BB (2011) A Facile Template Free Approach for the Large Scale Solid Phase Synthesis of CdS Nanostructures and

Their Excellent Photocatalytic Performance. Small 7:957-964

35. Ni M, Leung MKH, Leung DYC, Sumathy K (2007) A review and recent developments in photocatalytic water splitting using $TiO_2$ for hydrogen production. Renew SustEnerg Rev 11:401-425

36. Nolan MG, Hamilton JA, O'Brien S, Bruno G, Pereira L, Fortunato E, Martins R, Povey IM, Pemble ME (2011) The characterisation of aerosol assisted CVD conducting, photocatalytic indium doped zinc oxide films. J PhotochPhotobi A 219: 10–15

37. Murali A, Sarswat PK, Sohn HY (2019) Enhanced Photocatalytic Activity and Photocurrent Properties of Plasma- Synthesized Indium-Doped Zinc Oxide (IZO) nanopowder. Mater Today Chem 11: 60-68

38. Rezapour M, Talebian N (2014) Synthesis and investigation of Indium doping and surfactant on the morphological, optical and UV/Vis photocatalytic properties of ZnO nanostructure. Ceram Int 40: 3453–3460

39. Yu Y, Yao B, He Y, Cao B, Ma W, Chang L (2020) Oxygen defect-rich In-doped ZnO nanostructure for enhanced visible light photocatalytic activity. Mater ChemPhys 244: 122672

40. Ben Ameur S, BelHadjltaief H, Duponchel B, Leroy G, Amlouk M, Guermazi H, Guermazi S (2019) Enhanced photocatalytic activity against crystal violet dye of Co and IndopedZnO thin films grown on PEI flexible substrate under UV and sunlight irradiations. Heliyon 5: e01912

41. Tubtimtaea A, Lee MW (2012) ZnOnanorods on undoped and indium-doped ZnO thin films as a TCO layer on nonconductive glass for dye-sensitized solar cells, SuperlatticeMicrost 52: 987–996.

42. Dhamodharan P, Chen J, Manoharan C (2021) Fabrication of In doped ZnO thin films by spray pyrolysis as photoanode in DSSCs. Surf Interfaces 23: 100965

43. Khadtare S, Pathan HM, Han SH, Park J (2021) Facile synthesis of binder free ZnO and its Indium, Tin doped materials for efficient dye sensitized solar cells. J Alloys Compd 872: 159722

44. Chava RK, Kang M (2017) Improving the photovoltaic conversion efficiency of ZnO based dye sensitized solar cells by indium doping. J. Alloys Compd. 692: 67-76.

45. Mohamad IS, Norizan MN, Hanifiah MKFM, Amin IAM, ShahiminMM (2014) Fabrication and characterization of ZnO:In thin film as photoanode for DSSC using natural fruit dyes. AIP Conf. Proceed 1607: 070049 (1-6).

**Captions to Figures:**

**Figure 1:** (a) XRD patterns of pure ZnO and indium doped ZnO hierarchical nanostructures. (b) XRD in the range of 30-38° indicating shift in (002) reflection.

**Figure 2:** FESEM images of (a) ZnO, (b) 0.25% In@ZnO, (c) 0.5% In@ZnO, (d) 1% In@ZnO, (e) 2% In@ZnO and (f) 3% In@ZnO powder samples.

**Figure 3:** FETEM images corresponding to2 mol% In-ZnO sample at (a) low, (b) intermediate and (c) high magnification and (d) SAED pattern**.**

**Figure 4:** FETEM-STEM-EDS data corresponding to2 mol% In-ZnO sample

**Figure 5:** FETEM-STEM-EDS-Elemental mapping images of 2 mol% In-ZnO sample: (a) Electron images and corresponding elemental mapping images: (b) indium, (c) zinc and (d) oxygen.

**Figure 6:** (a) UV-Visible and (b) photoluminescence spectra of pure and indium doped zinc oxide hierarchical nanostructures.

**Figure 7:** Optimized atomic structure (left) and partial density of states (right) (a) ZnO, (b) $Zn_{0.97}In_{0.03}O$, and (c) $Zn_{0.94}In_{0.06}O$. (Atomic color code: Zn=grey; In=Green; O=red).

**Figure 8:** XPS study of In@ZnO (a) 3d spectrum of Indium (b) 2p spectrum of Zinc (c) is spectrum of oxygen.

**Figure 9: Photocatalytic** hydrogen generation *via* $H_2O$ splitting with plain ZnO and In@ZnO.

**Figure 10:** Current-voltage curve and IPCE of the DSSCs based on plain ZnO and In@ZnO.

**Captions to Table:**

**Table 1:** The $H_2$ generation rates for as synthesized ZnO (I) and In@ZnO.

**Table 2:** The Photovoltaic parameters derived from the *J-V* curves shown in Figure 10.

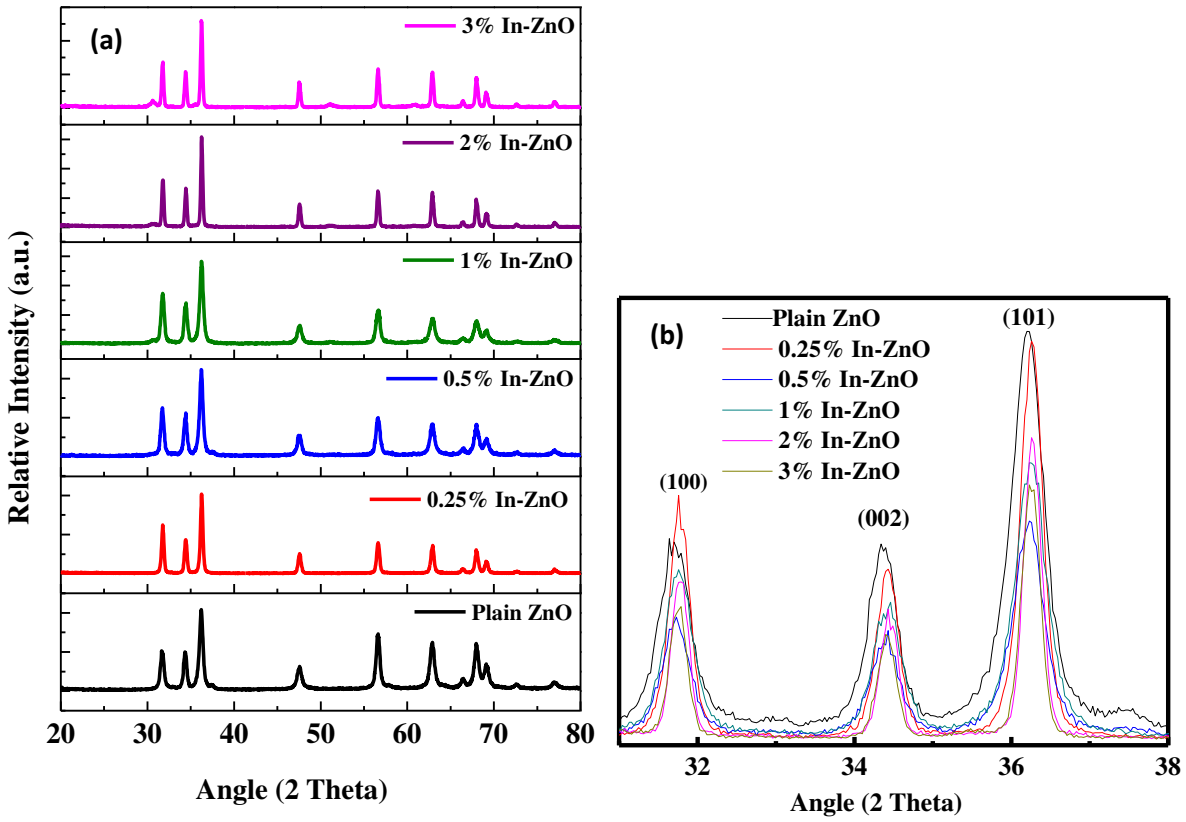


**Figure 1:** (a) XRD patterns of pure ZnO and indium doped ZnO hierarchical nanostructures. (b) XRD in the range of 30-38° indicating shift in (002) reflection.

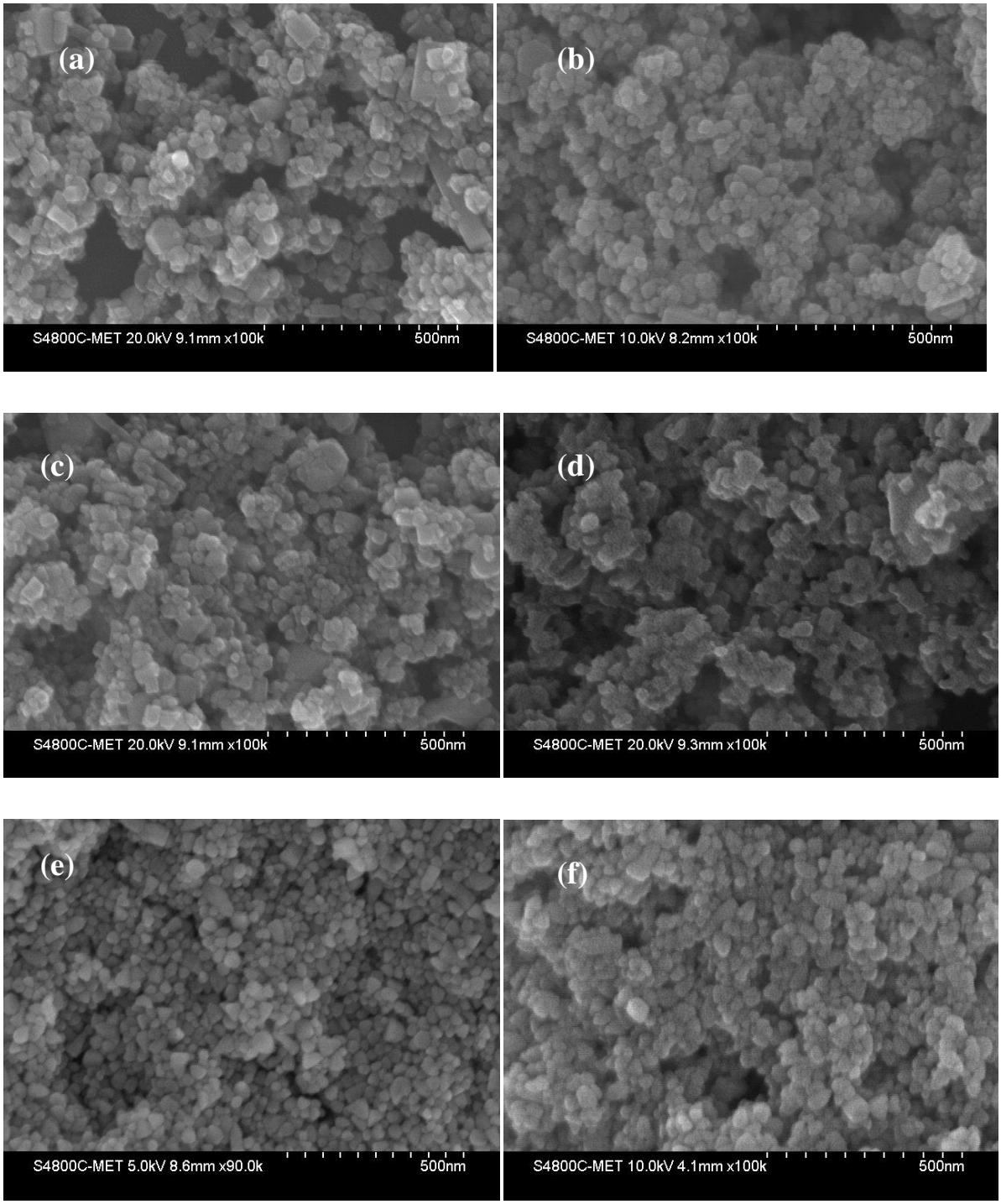


**Figure 2:** FESEM images of (a) ZnO, (b) 0.25% In@ZnO, (c) 0.5% In@ZnO, (d) 1% In@ZnO, (e) 2% In@ZnO and (f) 3% In@ZnO powder samples.

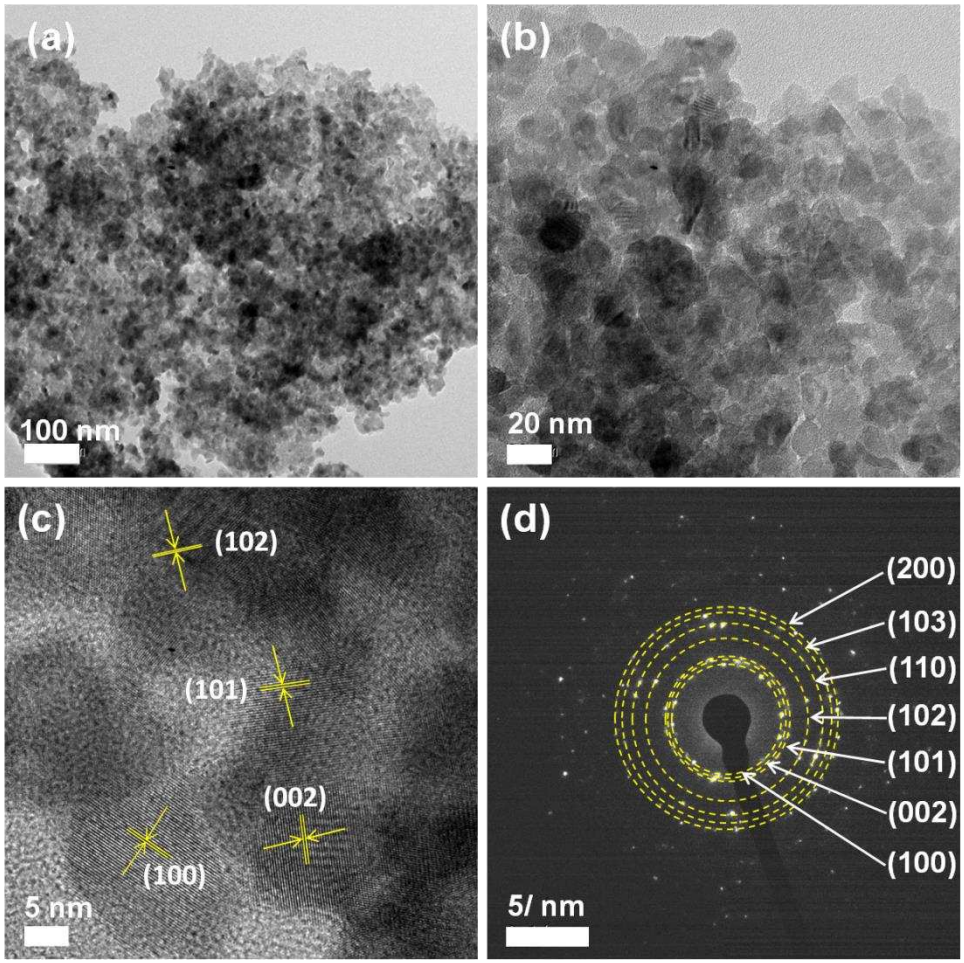


**Figure 3:** FETEM images corresponding to2 mol% In-ZnO sample at (a) low, (b) intermediate and (c) high magnification and (d) SAED pattern**.**

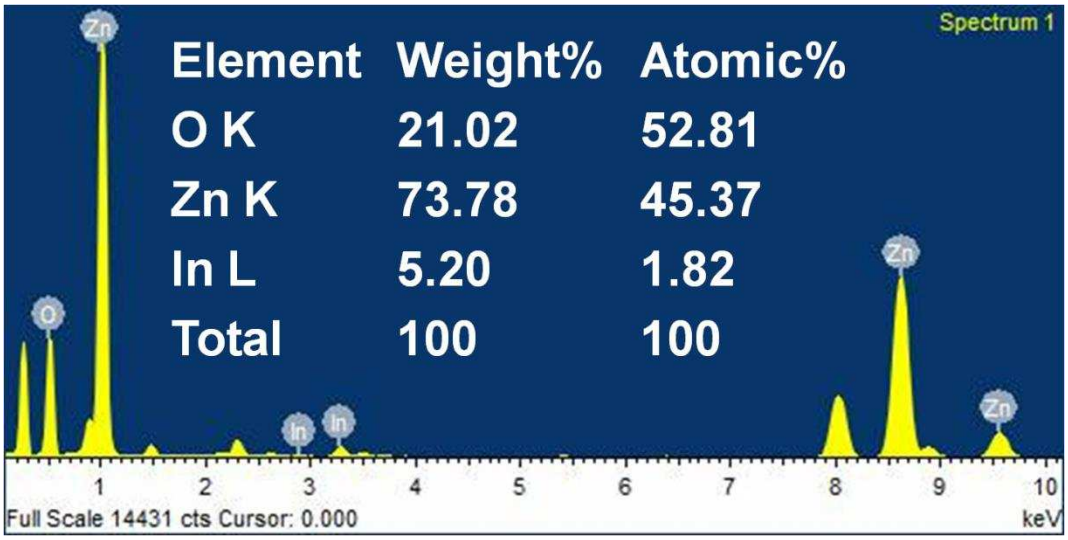


**Figure 4:** FETEM-STEM-EDS data corresponding to2 mol% In-ZnO sample.

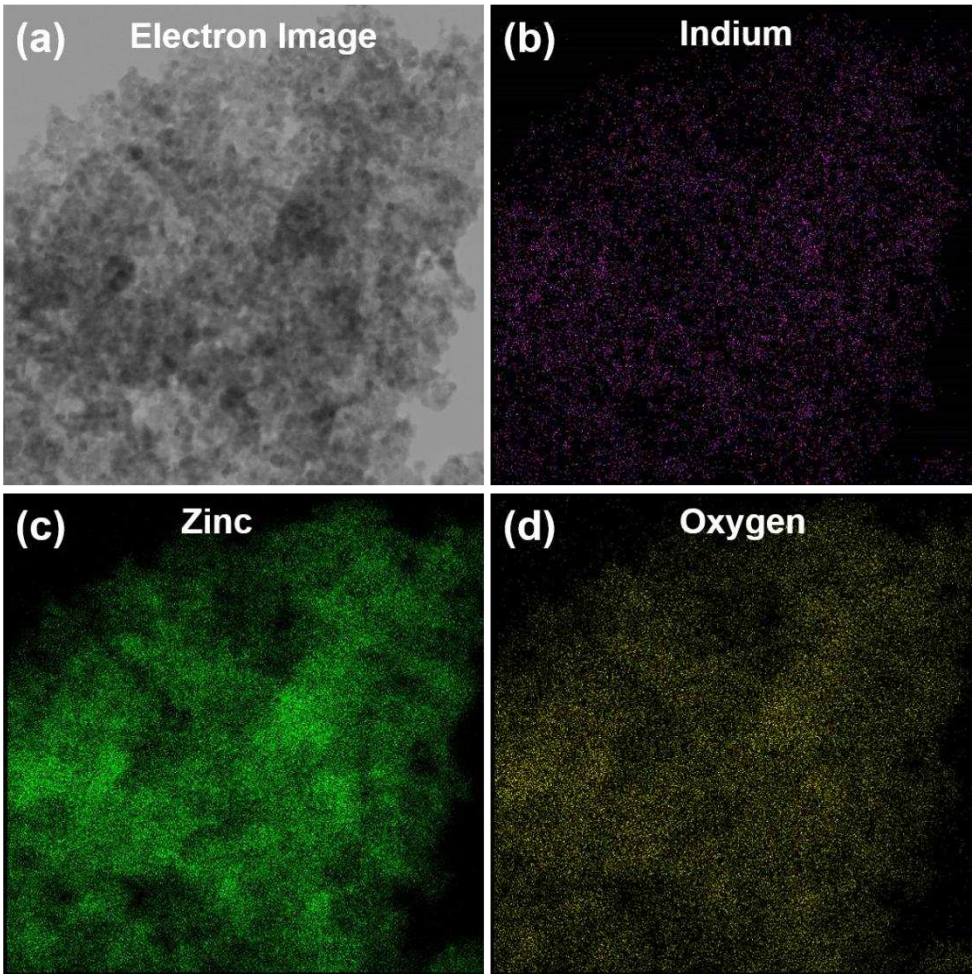


**Figure 5:** FETEM-STEM-EDS-Elemental mapping images of 2 mol% In-ZnO sample: (a) Electron images and corresponding elemental mapping images: (b) indium, (c) zinc and (d) oxygen.

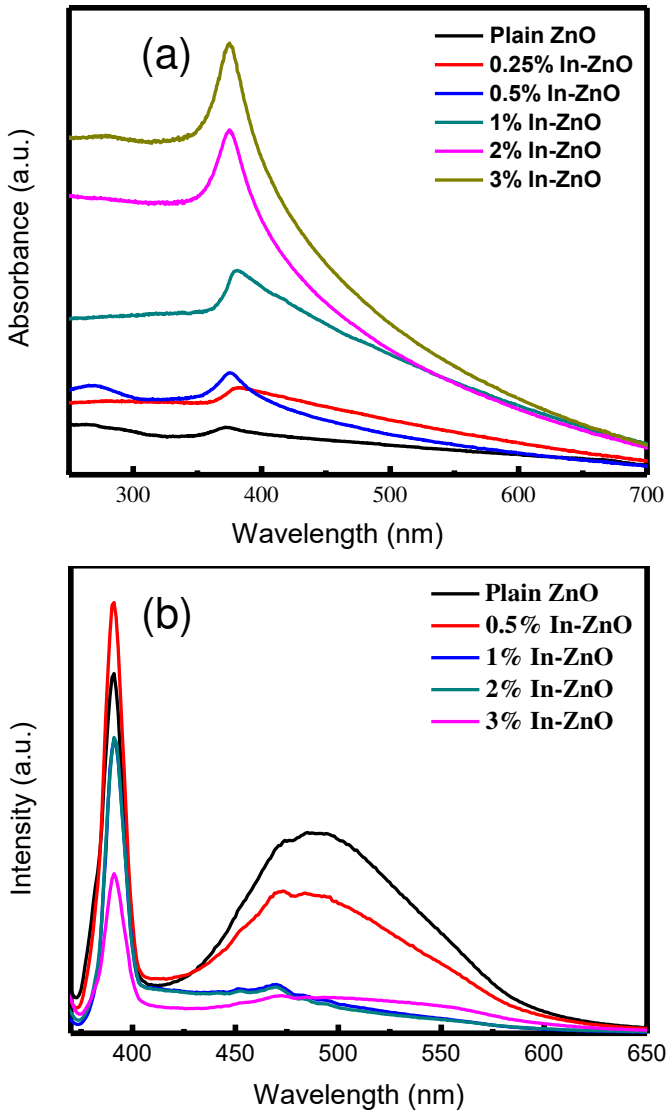


**Figure 6:**(a) UV-Visible and (b) Photoluminescence spectra of pure and indium doped zinc oxide hierarchical nanostructures.

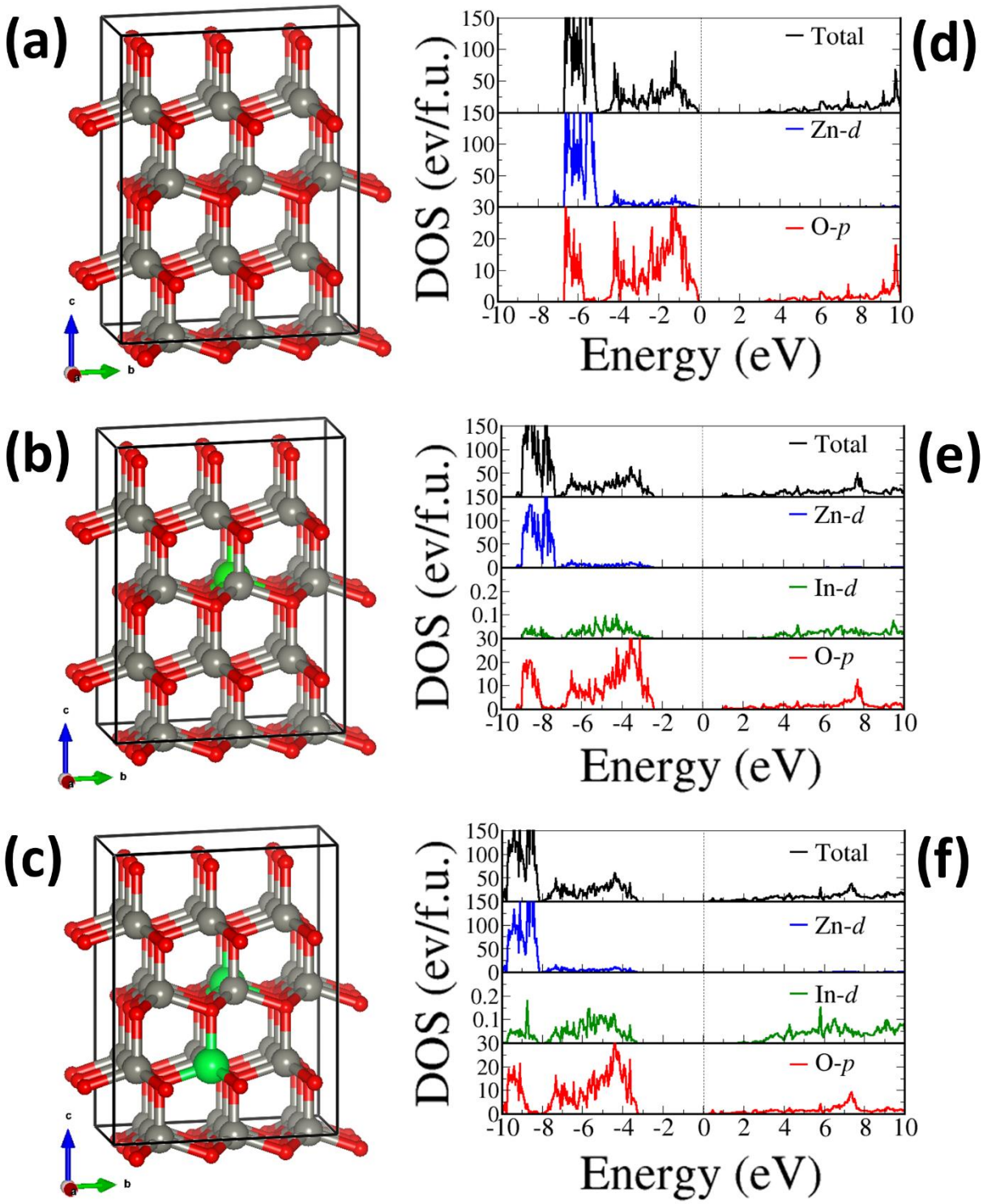


**Figure 7:**Optimized atomic structure (left) and partial density of states (right) (a) ZnO, (b) $Zn_{0.97}In_{0.03}O$, and (c) $Zn_{0.94}In_{0.06}O$. (atomic color code: Zn=grey; In=Green; O=red).

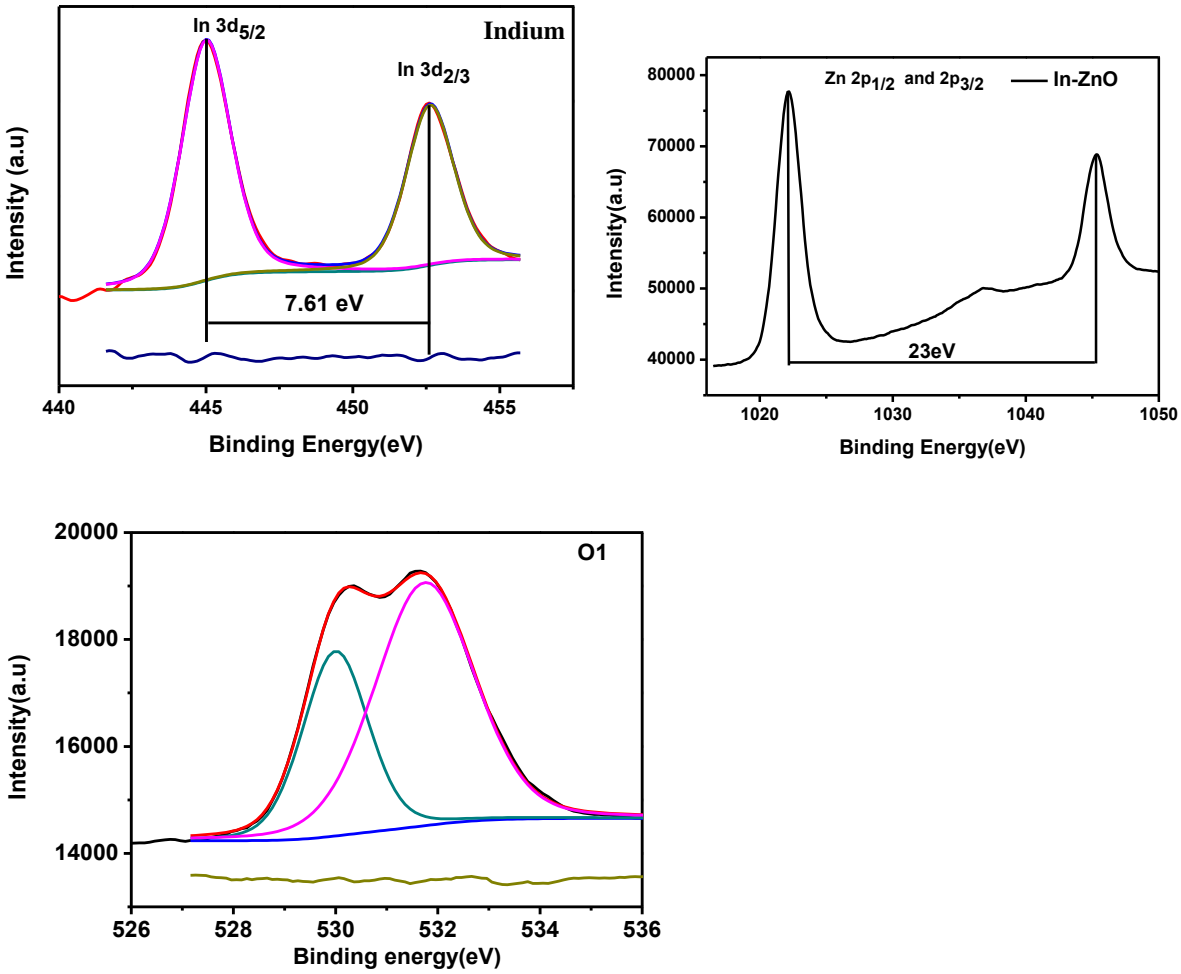


**Figure 8:** XPS study of In@ZnO (a) 3d spectrum of Indium (b) 2p spectrum of Zinc (c) is spectrum of oxygen.

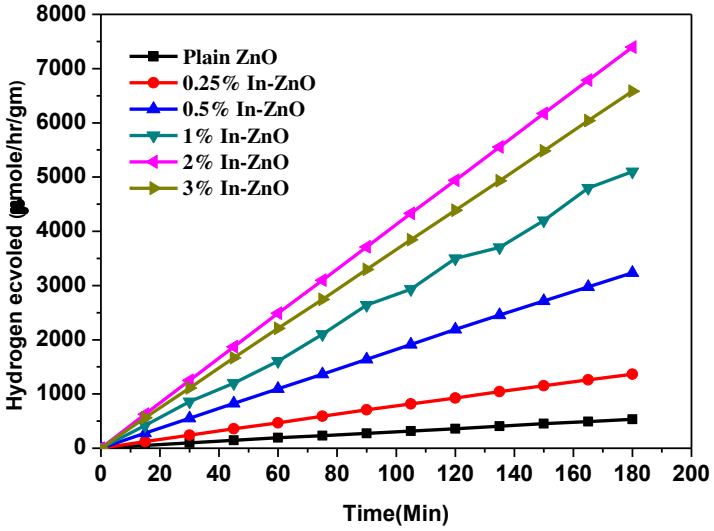


**Figure 9:**Photocatalytic hydrogen generation *via* $H_2O$ splitting with with plain ZnO and In@ZnO.

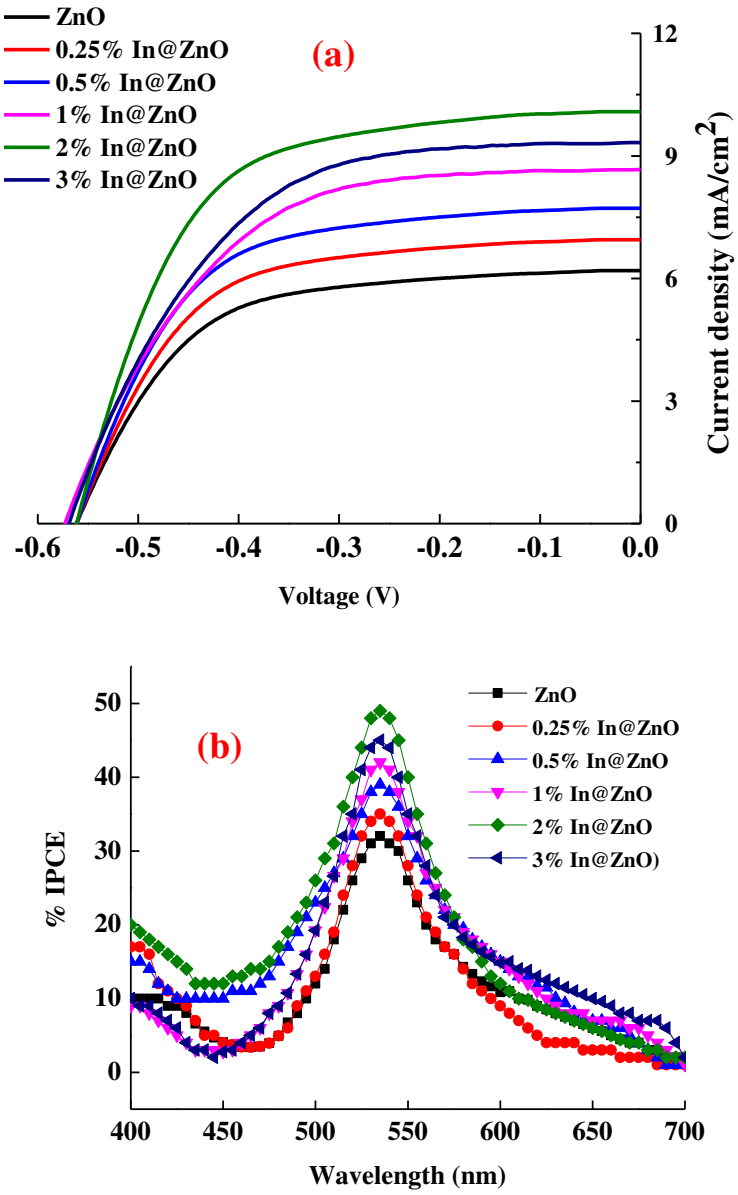


**Figure 10:** Current-voltage curve (a) and IPCE (b) of the DSSCs based on plain ZnO and In@ZnO.

**Table 1:** The $H_2$ generation rates for as synthesized (plain) ZnOand In@ZnO.

| Sr. No. | Sample | $H_2$ evolution rate (µmol/h/g) |
|---|---|---|
| 1 | Plain ZnO | 177 |
| 2 | 0.25%In@ZnO | 455 |
| 3 | 0.5%In@ZnO | 1078 |
| 4 | 1%In@ZnO | 1700 |
| 5 | 2%In@ZnO | **2465** |
| 6 | 3%In@ZnO | 2194 |

**Table 2:**The comparison of photovoltaic parameters of available reports with those derived from the *J-V* curves (shown in Figure 10) in the present work.

| **Sample** | $J_{sc}$(mAcm$^{-2}$) | $V_{oc}$ (V) | ***FF*** | ***η*(%)** | ***IPCE* (%)** | ***Ref.*** |
|---|---|---|---|---|---|---|
| In doped ZnO thin film | 2.82 | 0.600 | 0.65 | 1.09 | -- | 42 |
| In doped ZnONPs | 12.49 | 0.480 | 0.55 | 3.41 | -- | 43 |
| In doped ZnONPs | 12.58 | 0.421 | 0.51 | 2.70 | 51 | 44 |
| In doped ZnO thin film | 0.07 | 0.72 | 0.45 | 0.34 | -- | 45 |
| **Plain ZnO** | 6.19 | -0.558 | 0.61 | 2.11 | 32 | Present work |
| **0.25% In@ZnO** | 6.95 | -0.559 | 0.61 | 2.38 | 35 | --do-- |
| **0.5% In@ZnO** | 7.72 | -0.560 | 0.61 | 2.64 | 39 | --do-- |
| **1% In@ZnO** | 8.66 | -0.568 | 0.56 | 2.77 | 42 | --do-- |
| **2% In@ZnO** | 10.08 | -0.566 | 0.60 | 3.46 | 49 | --do-- |
| **3% In@ZnO** | 9.33 | -0.564 | 0.57 | 2.95 | 45 | --do-- |